Advances in Water Resources 144 (2020) 103711

Contents lists available at ScienceDirect

Advances in Water Resources

journal homepage: www.elsevier.com/locate/advwatres

A greyscale volumetric lattice Boltzmann method for upscaling pore-scale two-phase flow

Senyou An[a], Yuting Zhan[b], Jun Yao[c], Huidan Whitney Yu[d], Vahid Niasar[a,*]

[a] Department of Chemical Engineering and Analytical Science, University of Manchester, Manchester M13 9PL, UK
[b] Dyson School of Design Engineering, Imperial College London, South Kensington Campus, London SW7 2AZ, UK
[c] School of Petroleum Engineering, China University of Petroleum, Qingdao 266580, China
[d] Department of Mechanical Engineering, Indiana University-Purdue University, Indianapolis, IN 46202, USA

ARTICLE INFO

Keywords:
Volumatric lattice Boltzmann method
Level-set method
Pore-structure upscaling
Two-phase flow
GPU parallelisationpP

ABSTRACT

Solving image-based pore-scale flow and transport in porous materials is a mainstream of fundamental and industrial research to reveal the pertinent physics in the field of hydrogeology, reservoir engineering, paper and filter engineering. This research discipline requires tremendous integration of multidisciplinary research areas of image processing, computational fluid modelling, and high-performance computing. The key challenge in pore-scale multi-phase flow simulation is the overwhelming computational expense. In this paper, we develop a new computational method that integrates GPU-accelerated volumetric lattice Boltzmann method (VLBM) with an upscaling scheme to solve the pore-scale two-phase flow at the centimetre-level length scales. The lattice Boltzmann concept is employed to solve both the level-set equation for image segmentation and governing equations for multi-phase flow dynamics. The signed distance field solved from the level set equation is used to calculate the void volume ratio of each lattice cell, resulting in a seamless connection between image segmentation and computational fluid dynamics. The pore-scale porous materials upscaling is carried out through the average void volume ratio of the neighbouring cells. The algorithm is rigorously tested in three cases: contact angle test for droplets between two plates, co-current flow in a cylindrical tube, and the two-phase flow in a sandstone sample. For the sandstone sample, the porosity, void space topology, relative permeability and preferential flow channels are well retained after 8-times upscaling, while the computational time is dramatically decreased.

1. Introduction

Two-phase flow through porous materials is a common phenomenon encountered in the energy industry, e.g. reservoir engineering (Ramstad et al., 2010), geological carbon storage (Bruant et al., 2002) and fluid flow in fuel cells cells (Niblett et al., 2019). Given the advanced computational technologies, a very significant wealth of research has been dedicated to pore-scale simulations to improve in-depth understanding of the physics of fluids and enhance the predictive capability (Joekar-Niasar et al., 2012). Image-based experiments using optical (Godinez-Brizuela et al., 2017; Karadimitriou et al., 2017) or X-ray imaging (Gao et al., 2017; Tracy et al., 2015; Yang et al., 2020) have provided the opportunity to acquire the input data for pore-scale simulations and also to validate the pore-scale simulations of flow and transport problems (Aziz et al., 2018; Joekar-Niasar et al., 2010).

Pore-scale X-ray imaging, started back in 1991 (Dunsmuir et al., 1991) allow characterisation of multi-phase flow and transport down to 20 nm resolution. However, the scarcity of experimental data is an inevitable problem because experiments are usually time-consuming and costly and image processing is a very burdensome tedious task which in dynamic cases can end of tens of TB data size (Ramstad et al., 2010). Furthermore, the reproducibility of experiments at small scale samples (mm scale) is very challenging because of fluid contamination and serious challenges in controlling the boundary conditions. Thus, performing computational simulations based on the digital images of porous materials or designed structures is an alternative technology to overcome the aforementioned experimental challenges.

Pore-scale simulations started by pore-network modelling back in 1956 by Fatt (1956) have simulated two-phase flow, transport and more complex phenomena such as electro-migration in porous materials (An et al., 2020; Bakke and Øren, 1997; Cornelissen et al., 2019; Hasan et al., 2019; Joekar-Niasar and Hassanizadeh, 2012; Xiong et al., 2016). Since this method simplifies pore morphology to employ analytical expressions for physics of flow and transport, it is computationally cheap but cannot resolve flow and transport in exact pore morphology. This bottleneck becomes crucial if the ratio of the porous medium length scale

* Corresponding author.
E-mail address: vahid.niasar@manchester.ac.uk (V. Niasar).

https://doi.org/10.1016/j.advwatres.2020.103711
Received 6 May 2020; Received in revised form 26 June 2020; Accepted 30 July 2020
Available online 31 July 2020

to the pore size is very small (such as gas diffusion layer or papers which are very thin). The second category of simulation methods referred to the direct methods, use directly the images obtained from X-ray or optical imaging. In these methods, two-phase flow through porous materials can be solved by variations of Stokes or Navier-Stokes equations (An et al., 2016; Taylor and Hood, 1973). Before the simulation, the spatial dispersion for the pixels of void space can be realized based on the unstructured mesh, which is usually composed of tetrahedrons (Godine-Brizuela and Niasar, 2019). However, the natural porous materials typically have random and complex pore spaces, e.g. thin tips and small isolated space (An et al., 2017a). To avoid these challenging elements, they are usually smoothed in the previous literature (Raeini et al., 2014). Both segmentation and smoothing introduce non-negligible errors for the characterization of porous materials, which can be crucial for imbibition and film flow processes. Directly converting the pixels of pore space to the structured mesh is a simple but effective way, which, however, needs more grid cells and increases the computational demand (Ollivier-Gooch and Altena, 2002).

Using a structured mesh will provide the advantage of avoiding the smoothing procedure. Structured grids have been used in former volume-of-fluid based finite volume simulations on the OpenFOAM platform to simulate two-phase flow in porous materials (Raeini et al., 2012, 2014). A dynamic two-phase drainage simulation was reported to take approximately 13 days for one Berea sample with a grid size of 330 × 210 × 210 on a facility with 24 processors at a clock speed of 2GHz (Raeini et al., 2015). Lattice Boltzmann methods (LBM) are also suitable to simulate the complex flow in the complex structures using the structured grids because of their mesoscopic features (Boek and Venturoli, 2010; Ferreol and Rothman, 1995; Genty and Pot, 2013; Masoodi and Pillai, 2012; Pan et al., 2004; Ramstad et al., 2010; Wang et al., 2020; Zhao et al., 2016). Generally, LBM is a computationally demanding method. A single drainage simulation on 40 multiple computer processors (CPUs) takes about 30 h for a Berea sample with grid size 256 × 256 × 256 (Ramstad et al., 2012). Resulting from the properties of high-density calculation, the calculation speed of LBM can be effectively improved based on parallelization (An et al., 2017b). Furthermore, upscaling the pore-scale image is also an effective way to accelerate the calculation. Previous research shows that the simulation performance scales roughly linear as long as the number of grid blocks per processor is kept larger than 20,000 (Raeini et al., 2015). However, the methodology to accurately characterise the two-phase flow using less lattice is a challenge not being addressed in computational physics of multi-phase flow in porous materials.

This paper bears three novel aspects that contribute to porous materials research area:

(a) We improve the accuracy of structured mesh for the image-based pore-scale two-phase flow simulation. Active contour equations are solved to detect the solid boundaries, which is represented by distance field. Combining with local refinement method, the ratio of solid in each cell can be analyzed. In this schematic, the structured mesh is improved to have a more accurate representation of the grey fluid-solid interfaces.
(b) GPU-CUDA parallelization technology is used to accelerate the calculations based on the proposed volumetric lattice Boltzmann method (VLBM) for two-phase flow in porous materials. This method is based on the classical Shan-Chan multi-component multi-phase model (Shan and Doolen, 1995).
(c) A pore-scale upscaling method is proposed to reduce the number of lattice points. In this upscaling method, the average value of specific neighbour grids is calculated to represent the occupancy of solid and void space, which promotes the advantages of VLBM and improves the computational efficiency of structured mesh.

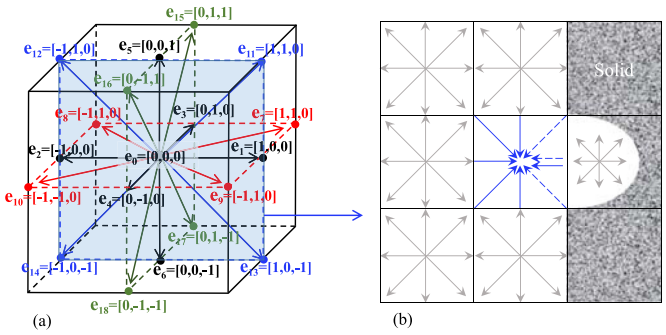

Fig. 1. (a) The D3Q19 model for lattice Boltzmann equation. D3Q19 means 3 dimensions and 19 directions. $e_i (i = 0 - 18)$is discrete molecular velocities in the 19 directions. (b) A schematic representation of streaming and bounce-back in VLBM. Grey colour lines represent the particle population at time *t*. Blue solid lines represent the streaming part from upwind sites. Blue broken lines represent the bounce-back part.

2. Computational methodology

In this section, we introduce four different topics including volumetric LBM used in our flow simulation, the level-set equation used in image segmentation, GPU-parallelized LBM schematic and the pore-scale upscaling algorithm.

2.1. Volumetric lattice Boltzmann method for two-phase fluid dynamics

The lattice Boltzmann method is an alternative way to directly solving Navier-Stokes equations used in fluid dynamics and has ubiquitous applications in engineering. For an accurate description of the complex solid-fluid interface, especially arbitrarily moving boundaries, single-phase volumetric LBM (Yu et al., 2014) was proposed based on the D3Q19 model. The D3Q19 model and responding discrete molecular velocities $\boldsymbol{e}_i (i = 0 - 18)$ are shown in Fig. 1a. For the typical node-based LBM, fluid is discretized to particle clusters and particles are allocated to the binary nodes (usually structured grids) by ignoring the node volume. As shown in Fig. 1a, if we set 0 being the host, 1 – 18 are neighbours. Unlike the typical node-based LBM, the fluid particles are assumed to have volume and the density is uniform in each lattice cell in the VLBM. VLBM has been applied to the simulation of moving boundary model, oil flow in sandstone and blood flow in artery and choroid capillaries (An et al., 2017a; 2017b; Yu et al., 2014; Gelfand et al., 2018; Wang et al., 2015), all of which are single-phase flow governed by Eq. (1).

$$n_i(\boldsymbol{x} + \boldsymbol{e}_i t, t + \Delta t) = n_i(\boldsymbol{x}, t) - \left[n_i(\boldsymbol{x}, t) - n_i^{eq}(\boldsymbol{x}, t)\right]/\tau \tag{1}$$

where $n_i(\boldsymbol{x}, t)$ represents the particle population in cell $\boldsymbol{x}$ and time t, $n_i^{eq}(\boldsymbol{x}, t)$ is the equilibrium particle population, index i is the predefined direction of molecular motion same with previous introduction, $n_i(\boldsymbol{x} + \boldsymbol{e}_i t, t + \Delta t)$ is the particle population after the one step evolution. τ is a relaxation time in the BGK model, which is related to the kinematic viscosity as shown in Eq. (2) (Guo et al., 2000). To improve the numerical stability, multi-relaxation time can be adopted for the collision processor (Premnath and Abraham, 2007).

$$\nu = c_s^2(\tau - 0.5\Delta t) \tag{2}$$

$$c_s = c/\sqrt{3} \tag{3}$$

where $c = \Delta \boldsymbol{x}/\Delta t = 1$ in lattice units by assuming unit values for lattice length $\Delta \boldsymbol{x}$ and time scale Δt. c_s represents the sound speed in lattice unites.

The equilibria of particle population is based on the D3Q19 model, so n_i^{eq} follows Eq. (4).

$$n_i^{eq}(\boldsymbol{x}, t) = N\omega_i\left(1 + \frac{3\boldsymbol{e}_i \cdot \boldsymbol{u}}{c^2} + \frac{9(\boldsymbol{e}_i \cdot \boldsymbol{u})^2}{2c^4} - \frac{3\boldsymbol{u}^2}{2c^2}\right) \tag{4}$$

$$\omega_0 = 1/3,\ \omega_{1-6} = 1/18,\ \omega_{7-18} = 1/36 \tag{5}$$

where ω_i is the weighting factors, N represents the macro-scale density by summarizing the particle population in all directions shown in Eq. (6), $\boldsymbol{u}$ is the velocity vector calculated using Eq. (7).

$$N(\boldsymbol{x},t) = \sum_{i=1}^{b} n_i(\boldsymbol{x},t) \tag{6}$$

$$\boldsymbol{u}(\boldsymbol{x},t) = \sum_{i=1}^{b} \boldsymbol{e}_i n_i(\boldsymbol{x},t)/N(\boldsymbol{x},t) \tag{7}$$

The ratio of solid volume to lattice volume, $\mathcal{P}(\boldsymbol{x})$, is considered in the VLBM to more accurately express the complex solid boundaries in the porous materials, compared with the binary grid (An et al., 2017a). With the consideration of volume concept in the VLBM, the solution of Eq. (1) will differ, compared to the traditional node-based LBM. For a rigid boundary, the collision term is similar to the node-based LBM, as shown in Eq. (8).

$$n_i'(\boldsymbol{x},t) = n_i(\boldsymbol{x},t) - \left[n_i(\boldsymbol{x},t) - n_i^{eq}(\boldsymbol{x},t)\right]/\tau \tag{8}$$

where $n_i'(\boldsymbol{x},t)$ is the post-collision particle population.

Although the collision operator in VLBM and node-based LBM are similar, streaming operation in VLBM is different from the node-based LBM due to the partial occupancy of solid/fluid in a grey boundary cell.

$$n_i''(\boldsymbol{x},t+\Delta t) = [1-\mathcal{P}(\boldsymbol{x})]\cdot n_i'(\boldsymbol{x}-\boldsymbol{e}_i\Delta t,t) + \mathcal{P}(\boldsymbol{x}+\boldsymbol{e}_{i^*}\Delta t)\cdot n_{i^*}'(\boldsymbol{x},t) \tag{9}$$

where $n_i''(\boldsymbol{x},t)$ is the post-streaming particle population, i^* represents the direction opposite to the ith direction. In each evolution step, the post-streaming particle population is updated after collision. As partial occupation of fluid in the grey boundary cells, a fraction of the fluid particles is transferred from the upwind neighboring cells, $[1-\mathcal{P}(\boldsymbol{x})]\cdot n_i'(\boldsymbol{x}-\boldsymbol{e}_i\Delta t,t)$. When the particles stream to the downwind cells, parts of them are bounced back if the downwind cells are not pure fluid cells, as shown in Fig. 1b. The ratio of converted particles can be calculated using $\mathcal{P}(\boldsymbol{x}+\boldsymbol{e}_{i^*}\Delta t)\cdot n_{i^*}'(\boldsymbol{x},t)$. Considering the partialstreaming is the main highlight in the VLBM.

To extend the VLBM to two-phase flow, the classic multi-component multi-phase Shan-Chen LBM model (Shan and Doolen, 1995) is adopted in this paper as it is computationally efficient. More complex models (e.g. high-density high-viscosity ratio model) can also be combined with the concept of VLBM in the same way. In the Shan-Chen model, the phase separation can be thought of as a hydrophobic interaction, e.g. immiscible water and oil. The algorithm needs two or more indices σ to traverse the fluid components. Each of phase components satisfies the governing Eq. (1), (4) and (9). The macroscopic velocity $\boldsymbol{u}_\sigma^{eq}$ differs from the macroscopic uncoupled velocities, as Eq. (10).

$$\boldsymbol{u}_\sigma = \boldsymbol{u}' + \frac{\tau_\sigma \boldsymbol{F}_\sigma}{\rho_\sigma} \tag{10}$$

where ρ_σ is the density of phase σ, which is calculated in the same way as with the single component model. $\boldsymbol{u}'$ is a velocity common to the various components as defined in Eq. (11). It represents the flow of the bulk fluid and, as such, is the physical velocity entity to analyze for the overall fluid flow.

$$\boldsymbol{u}' = \frac{\sum_\sigma \frac{1}{\tau_\sigma}\sum_\sigma f_i^\sigma \boldsymbol{e}_i}{\sum_\sigma \frac{\rho_\sigma}{\tau_\sigma}} \tag{11}$$

From Eq. (10), we can see that the force acting is one component of velocity $\boldsymbol{u}_\sigma$. Theoretically, the parameter $\boldsymbol{F}_\sigma$ can include any force affecting flow. By neglecting gravity, we consider the effect of interaction chemical forces to the two-phase flow system, shown in Eq. (12).

$$\boldsymbol{F}_\sigma = F_{c,\sigma} + F_{ads,\sigma} \tag{12}$$

where $F_{c,\sigma}$ is the fluid-fluid cohesion and $F_{ads,\sigma}$ represents fluid-solid adhesion. Martys and Chen (1996) proposed the definition for cohesion and adhesion forces, as shown in Eq. (13).

$$\begin{aligned} F_{c,\sigma} &= -G_c\psi_\sigma(\boldsymbol{x},t)\sum_i \omega_i\psi_{\bar\sigma}(\boldsymbol{x}+\boldsymbol{e}_i\Delta t,t)\boldsymbol{e}_i \\ F_{ads,\sigma} &= -G_{ads,\sigma}\psi_\sigma(\boldsymbol{x},t)\sum_i \omega_i s(\boldsymbol{x}+\boldsymbol{e}_i\Delta t,t)\boldsymbol{e}_i \end{aligned} \tag{13}$$

where G_c is a parameter that controls the strength of the cohesion force between phase σ and phase $\bar\sigma$. For estimation of G_c, the threshold value $G_{c,crit} = 1/(\rho_1+\rho_2)$ and a representative density ρ_i were proposed (Huang et al., 2015). Based on the calculations, $G_c\rho_i = 1.8$ is an ideal state for an impressible fluid. $G_{ads,\sigma}$ is used to adjust the adhesion strength between fluid and solid wall particles. The parameter, $s(\boldsymbol{x}+\boldsymbol{e}_i\Delta t,t)$ is the indicator function of solid, equaling 1 or 0 for solid and fluid in traditional node-based binary LBM. To model surface tension forces in multicomponent fluids, Martys and Chen assume that $G_{\sigma,\bar\sigma}$ involves only nearest-neighbor interactions for simplicity (Martys and Chen, 1996).

To combine with the concept of the VLBM, we modify the force terms to satisfy the partialsolid occupation in lattice cells. As the fluid particles are uniformly distributed in the lattice cells in the VLBM, the occupation of fluid and solid in the nearest neighbours should be involved in the calculation of interaction potential. We add solid ratio $\mathcal{P}(\boldsymbol{x})$ into the Eq. (13) to get Eq. (14). ψ_σ and $\psi_{\bar\sigma}$ are commonly taken as the densities, $\psi_\sigma = \rho_\sigma$ and $\psi_{\bar\sigma} = \rho_{\bar\sigma}$.

$$\begin{aligned} F_{c,\sigma} &= -G_c\rho_\sigma(\boldsymbol{x},t)\sum_i \left[\omega_i\cdot\left(1-\mathcal{P}(\boldsymbol{x}+\boldsymbol{e}_i\Delta t)\right)\cdot\rho_{\bar\sigma}(\boldsymbol{x}+\boldsymbol{e}_i\Delta t,t)\cdot\boldsymbol{e}_i\right] \\ F_{ads,\sigma} &= -G_{ads,\sigma}\rho_\sigma(\boldsymbol{x},t)\sum_i \left[\omega_i\cdot\mathcal{P}(\boldsymbol{x}+\boldsymbol{e}_i\Delta t)\cdot\boldsymbol{e}_i\right] \end{aligned} \tag{14}$$

Young's equation, $\cos\theta = (\sigma_{S2}-\sigma_{S1})/\sigma_{12}$, is used to determine the contact angle considering interfacial tension between the two fluids σ_{12} and between each fluid and solid surface σ_{S1} and σ_{S2}. Young's equation can be simply reformulated by replacing the interfacial tensions by adhesion parameters $G_{ade,1}$ and $G_{ade,2}$ and the density factor $G_c(\rho_1+\rho_2)/2$, following (Huang et al., 2007):

$$\cos\theta_1 = \frac{G_{ads,2}-G_{ads,1}}{G_c\frac{\rho_1-\rho_2}{2}} \tag{15}$$

The velocity distribution has been transferred from mesoscopic parameter in the update of discrete molecular velocities. To get pressure distribution, the pressure is transferred based on Euler equation, as shown in Eq. (16). Considering two fluid phases, overall density is calculated $\rho = \rho_\sigma + \rho_{\bar\sigma}$.

$$p = c_s^2\rho + c_s^2 G_c\rho_\sigma\rho_{\bar\sigma} \tag{16}$$

As shown in the *Evolution Kernel* of Fig. 2, the algorithm includes five parts, namely *Streaming, Hydrodynamics update, Force calculation, Collision* and *Boundary update*. After setting initial condition, the *Streaming* was operated based on Eq. (9) for all fluid components. Then the density and velocity of each phase were calculated using Eqs. (6), (7), (10) and (11) to realize *Hydrodynamics update*. Following the update of hydrodynamics, *Force calculation* between different fluids were calculated based on Eqs. (12)–(15). With all updated macroscopic parameters, the *Collision* was done based on Eqs. (4) and (8). Finally, the *Boundary update* at inlet and outlet were realized using the nonequilibrium extrapolation scheme (Guo et al., 2002; Yin and Zhang, 2012).

2.2. Level-set method for image segmentation

As introduced in the Section 2.1, the VLBM needs an accurate solid ratio of boundary lattices, which can not be satisfied using the traditional binary segmentation method. Thus, an algorithm of image segmentation for porous materials was proposed based on the level-set

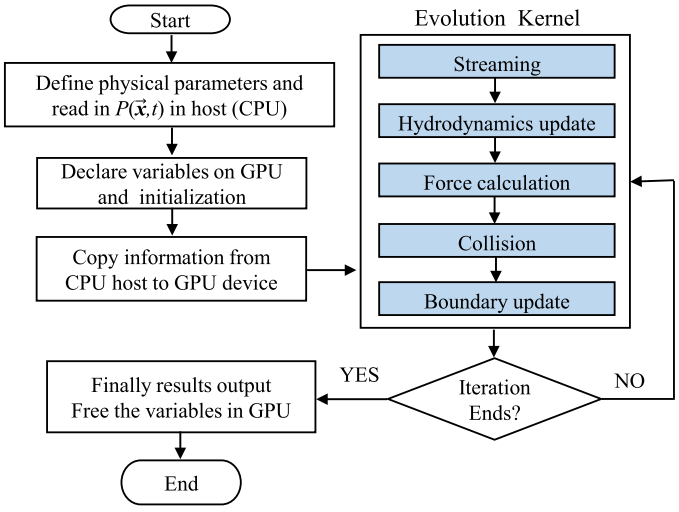

Fig. 2. The flow chart of the GPU parallelism of VLBM. The white order clusters are finished in the CPU host and the blue part is one the kernel on the GPU device. (For interpretation of the references to colour in this figure legend, the reader is referred to the web version of this article.)

method (An et al., 2017; Wang et al., 2015). For brevity, we do not provide a detailed description for image segmentation.

In this paper, the X-ray image was first enhanced using local- and cross-threshold methods to remove shading artefact and facility-caused outlier points. Then, Gauss smoothing method (Katz, 2016) was used to reduce the noise. After pre-processing the images, the level-set method (LSM) was adopted to detect the contour of pore space (Sethian, 1999). LSM used a discretized PDE to simulate the evolving of active contours by updating the fronts in porous materials until the stop condition was satisfied. The signed distance $\phi(\boldsymbol{x}, t)$ was defined for the enhanced image in the objective void space. The distance field evolution with time $\partial\phi/\partial t$ is shown as Eq. (17).

$$\partial\phi/\partial t = \nabla\cdot(g\nabla\phi) + \beta g \tag{17}$$

where g is a stopping function, defined as the gradient of a convolution $1/(1+|\nabla G\times I_0|^2)$. I_0 represents the gray-value distribution of X-ray image, and G is a Gaussian kernel. β is an adjustable constant value (Mitiche and Ayed, 2010).

The D3Q7 LBM concept was employed to discretize the level set equation as it can be considered a nonlinear diffusion equation with a source term (Wang et al., 2011). Similar to Eq. (1), the discretized LSE is written as Eq. (18).

$$h_i(\boldsymbol{x}+\boldsymbol{e}_i t, t+\Delta t) = h_i(\boldsymbol{x},t) - \left[h_i(\boldsymbol{x},t) - h_i^{eq}(\boldsymbol{x},t)\right]/\tau_\phi + \Delta t\cdot F_i(\boldsymbol{x},t) \tag{18}$$

where $h_i(\boldsymbol{x}, t)$ represents the discretized distribution of distance field $\phi(\boldsymbol{x})$ along direction $\boldsymbol{e}_i(\boldsymbol{x}, t)$, and $\phi(\boldsymbol{x}) = \sum_i h_i(\boldsymbol{x})$. $h_i^{eq}(\boldsymbol{x}, t)$ is the equilibrium state of $h_i(\boldsymbol{x}, t)$, defined as $h_i^{eq}(\boldsymbol{x}, t) = \phi(\boldsymbol{x}, t)/7$. $F_i(\boldsymbol{x}, t)$ is the external force, leading equation to balance state, and $F_i(\boldsymbol{x}, t) = \beta g/7$. Relaxation time τ_ϕ is defined as $\tau_\phi = 0.5 + 3g\Delta t$. The lattice time step Δt is usually set 1 (Guo et al., 2000).

After each collision and streaming operations, the distance function and the corresponding equilibrium distance distribution function were updated until reaching the balanced state. During the segmentation, one initial seed is usually used in the active contour method. One initial seed is suitable for continuous space, even the space contains bifurcations or intersections. This initial condition, however, is not suitable for porous materials. Because porous materials usually contain several paralleled or interconnecting pathways. Contour boundary cannot go through a solid phase, meaning just one initial contour will lose part of image information during the segmentation. Multi-point initial seed was proposed in this paper to solve this problem. After segmentation, the contour of the boundary was segmented by local refinement method to get the occupancy ratio of void space in the grey boundary cells.

2.3. GPU parallel computing

It has been well demonstrated that LBM and VLBM are ideally suited for GPU parallel computing (An et al., 2017b; Li et al., 2003). The principle and optimization of GPU parallelism in single-phase flow based on the VLBM was introduced in An et al. (2017b) and the acceleration time was more than one thousand times compared with single-CPU simulation. Comparing against the single component model, the streaming and collision are iterated for both fluids in the two-component model, and the Shan-Chen force term should be updated in every step. As shown in Fig. 2, the GPU parallelism of the two-phase algorithm has a scheme similar to the single-phase model.

As host, the CPU reads data and does variable allocation at the beginning of the algorithm. In this process, the logically contiguous heap memory is generated for global variables. Only contiguous memory can be used to carry out the location transfer between GPU and CPU. At the GPU device, we organize the algorithm structure and data structure to realize optimal parallelization. As shown in Fig. 2, the algorithm structure is streamlined into two kernels: one includes streaming and hydrodynamic update, and the other one includes force calculation, collision and boundary update. In each kernel, the global parameter is loaded once to decrease the time to access the global memory. Accessing the global parameter is one of the most time-consuming parts in a kernel while accessing a register (on-chip memory) consumes zero clock cycles per instruction in most cases. Optimized algorithm structure and arrangement of the register are central points in the improvement of parallel efficiency. The other optimal point is a data structure, which determines the way how to access global memory. The Structure of Array (SoA) data format is utilized in this paper to addresses the recall of coalesced global memory (An et al., 2017b).

2.4. Upscaling pore-scale VLBM

In addition to the GPU acceleration, upscaling the grid size is also an efficient approach to decrease the computational cost for numerical simulations. In the macro-scale numerical simulations for a reservoir, *effective properties* are usually used to reduce the computational cost by retaining the main features (Christie, 1996; Christie and Blunt, 2001; Salehi et al., 2019). To maintain different objective parameters, various averaging methods are specifically adopted, e.g. arithmetic average for porosity, harmonic average or geometric average for effective permeability and their combining procedures. Consequently, one can carry out calculations using a coarse grid to reduce computation time, making it possible to resolve larger domains.

The scale of a few pores is no exception to having the demand to reduce computation time. With the development of X-ray scanning technology and multiscale imaging methods, we can obtain fine pore-scale images (nano-scale resolution). The resolution of the X-ray micro-CT images in this study is around 3.7 μm. Supposing we want to make a comparative numerical study of pore-scale flow to a laboratory experiment on the centimetre scale, the grid size of the simulation domain will be about billion-level. Considering the processing power and memory requirement, it is difficult for common lab computational facilities to satisfy the computational demanding of pore-scale multi-phase flow simulation on a centimetre scale. As the size of image data describing the same area increases dramatically, how to effectively utilize this information without increasing the computational consumption is challenging. In this section, we propose a pore-scale structure upscaling method to reduce the computation grid size.

The upscaling method is proposed to replace the fine resolution pore-structure segmented from imaging data by a coarse resolution pore structure based on the averaged solid ratio, which is the geological feature of lattice in the VLBM. We can perfectly realise the volume preser-

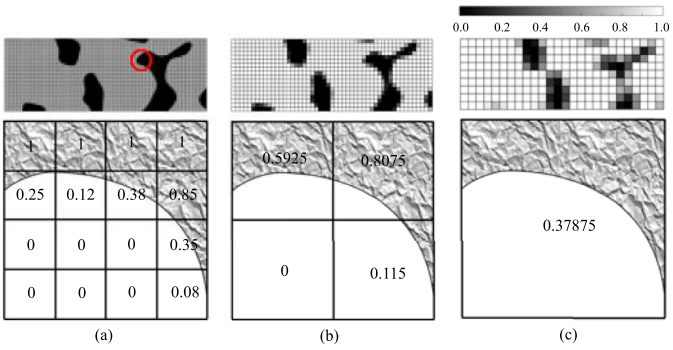

Fig. 3. The 2D slices of a porous material at different resolution (An et al., 2017a). (a) The original image at the resolution of 3.7μm/pixel. (b) and (c) Upscaled images 4 × and 16 ×, respectively. In the 3D samples, (b) and (c) are coarsened 8 × and 64 ×, respectively. The three images at the bottom show the zoom-in view of the red circle area from the top left figure. (For interpretation of the references to colour in this figure legend, the reader is referred to the web version of this article.)

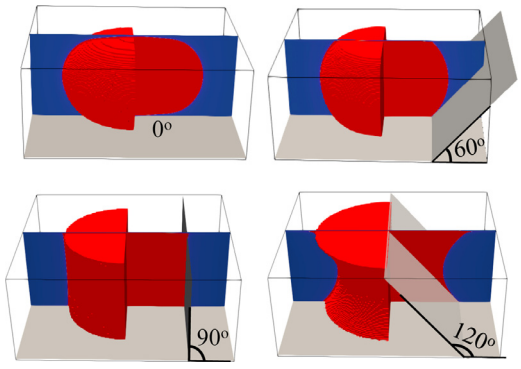

Fig. 4. Three-dimensional visualisation of a droplet sandwiched between two identical planes while surrounded by another immiscible fluids. Surface energies for both fluids have been changed such that the contact angle varies from 0° to 120°. The boundary cells' $\mathcal{P}$ for the planes are set 0.2.

vation during the pore-structure upscaling, meaning the porosity feature keeps identical in the equivalent pore structure. The geological and physical properties also remain similar until the main flow tunnels merge.

To better illustrate the pore-structure upscaling method, we choose one 2D sub-sample from the original 3D sample to represent fine-resolution and coarse-resolution samples, as shown in Fig. 3. From the image segmentation, the fine pore structure (Fig. 3a) is represented by the solid ratio function $\mathcal{P}$. Each mesh cell is labelled by a $\mathcal{P}(\boldsymbol{x})$ value distinguishing solid cell ($\mathcal{P}=1$), fluid cell ($\mathcal{P}=0$) and the boundary cell ($0<\mathcal{P}<1$). The upscaling ratio in each direction should be identical. A cubic upscaling domain is designed for the adjacent cells to realise specific upscaling time (e.g. the side length of the cubic domain is twice than lattice length to upscale 8 times for the original image, as shown in Fig. 3b). The solid occupation in the upscaled lattice cell is calculated by averaging the $\mathcal{P}$ value of fine cells. If both fluid and solid cells are included in an upscaled cell, the substitute cell will become a boundary cell. By changing the size of the cubic upscaling domain, we are able to continuously adjust the grid size of the image. The lattice size of Fig. 3c is 64 times bigger than the original image. Although the grid becomes coarse, the feature of pore structure (solid ratio and void space shape) is well retained, thus other macroscale parameters (absolute permeability, relative permeability) can be sufficiently preserved.

Excessively upscaling may cause the merge of main flowing pathways with the loss of the void space topology. While the porosity of porous materials is preserved, flow properties can not be reflected in the excessively upscaled sample. As a result, the maximum upscaling time should be tested for a new sample by choosing a representative element sub-volume. Because the degree of pore-structure upscaling is limited by the original resolution of images as well as the size of the smallest pores which are in the main flow pathways (the porosity and heterogeneity at the macro scale).

3. Application studies

This section is centred on the validation of two-phase VLBM and the upscaling results of two-phase flow in a sandstone. The computation tasks are carried out on an NVIDIA Tesla P100 GPU card, which has 3584 CUDA cores with 1190 MHZ clock frequency and 16 GB of global memory. To evaluate the GPU parallel performance, the serial computation is performed with Intel x86-64 CPU, which has 16 computing cores operating at 1.87 GHz and 64 GB DDR3 Random Access Memory (RAM).

3.1. Validation of two-phase VLBM

As introduced in the Section 2.1, the two-phase VLBM method based on the Shan-Chan model mainly includes 5 parts: streaming, collision, updating macro-scale parameters, updating boundary conditions and Shan-Chen force. The first four items have been certificated in the single-phase VLBM (An et al., 2017a), which are identical equations in the two-phase flow model. The parameter which should be validated in this paper is the modified Shan-Chen force for VLBM. From Eq. (14), the contribution of the neighbour cell is a function of solid ratio $\mathcal{P}$. To test our mathematical model, a series of droplets between two plates are designed and the static contact angles are measured under different interface conditions. In all of the regions occupied by wetting or nonwetting fluid, the fluids have the initial lattice density of 8.0 and initial complementary density 0. The two fluids have relaxation times $\tau_1=\tau_2=1$. Therefore the cohesion parameter can be calculated $G_{c,crit}=1/8$ and $G_c=0.225$. Using Eq. (15), the adhesion parameters are the only unknown variables. Assuming $G_{ads,2}=-G_{ads,1}$, we can change the contact angle via adjusting adhesion parameters as shown in Fig. 4, with $G_{ads,2}=-G_{ads,1}=0.45,\ 0.225,\ 0,\ -0.225$ to represent the corresponding contact angles 180°, 120°, 90° and 60°, separately.

For the test of modified force, the surfaces of plates are set 0.2 to represent the partial solid occupancy in VLBM. The simulation results show good fitting with pre-established measuring boards. For quantitative comparison of the contact angles, we calculate the contact angles from measurements of the base L and height H of the spherical curve on a surface. The radius R can be calculated $R=L^2/8H+H/2$. So the contact angle θ can be deduced $\cos\theta=\frac{L/2}{R}$. 0° and right angle are just total same as the curve detection based on the junction points. Other two cases are 59.9° and 120.0°, separately.

During immiscible two-phase flow in porous materials, both phases exist and flow in the same channel. For co-current annular two-phase flow in a cylindrical, we can assume that the nonwetting fluid is in the middle of the pore and wetting fluid creates a thin layer between the solid wall and the nonwetting fluid. For such a geometry, Eq. (19) can be used to estimate the relative permeability for the wetting and nonwetting phases (Ramstad et al., 2010).

$$k_r^w = S_w^2$$
$$k_r^{nw} = 2S_{nw}M + S_{nw}^2(1-2M) \tag{19}$$

where M is the viscosity ratio $M=\mu_{nw}/\mu_w$. We set identical viscosity for both phases, $M=1$. The analytical solution for concurrent flow is illustrated in Fig. 5.

Based on the local refinement method (An et al., 2017a), we generate the cylindrical tube and use grey cells $0<\mathcal{P}<1$ to describe the solid occupation of boundary cells. The sub-figures in Fig. 5 illustrate the dif-

ference between continuous data and binary data. For the binary data, vertical boundaries separate the fluid and solid, while the transitional grey area exists in the continuous data. Then we perform the simulations for different resolution levels. For the binary data, the model with a radius 40 lattices can ideally match the analytical solution, and coarsening the grid would increase the deviation from the analytical solution. For the continuous data, the simulation results can still fit the analytical solution even with a radius of 10 lattices. In a real porous medium, the radius of one pore in sandstone is usually less than 10 pixels under current imaging technology and computing level, which means the binary data in low resolution cannot accurately describe the flow.

From the validation of 3D cylinder, it can be seen that one advantage of continuous data is its accurate characterization of boundary by grey values. In addition, the upscaling of the structure is tested in this sample. With the decrease of grid size, the accuracy of simulation can still be guaranteed by maintaining the boundary information in the coarse sample.

3.2. Upscaling in a digital core

In this section, we analyze the efficiency of VLBM-based upscaling and the applicability of pore-structure upscaling in the course of solving pore-scale flow in a digital core. The micro-CT (MicroXCT-400) facility was operated to scan a man-made sandstone sample with resolution 3.7 μm/*pixel*. Since different phases have different X-ray absorption coefficients, the output of the scanning is a grey-scale image (dark pixel represents void space). A 256 cubic pixel sub-sample is cut from the original image for segmentation. Before segmentation, a local threshold and Gauss smooth method are applied to enhance the quality of the raw image. Next, the GPU-paralleled LBM-based level-set model is applied in this digital rock to capture the contour of the boundary using a distance field. After segmentation, we refine the lattices to accurately scatter the distance field and calculate the solid ratio function $\mathcal{P}$, which realizes a seamless connection with the VLBM for simulations.

Upscaling the structure sample from 256^3 to 128^3, 85^3, 64^3 and 32^3, the pressure distribution and absolute permeability show that the pore-structure upscaling can retain the identical absolute permeability up until 128^3 (8 times) (An et al., 2017a). As the structure values in VLBM are continuous, we can upscale the sample in a continuously variable level. Assuming the original resolution of one porous material sample is only fine enough to upscale total twice the size, the level of upscaling in every coordinate direction will be 1.26 times the grid size. For different samples, we can first cut representative element volume to determine the appropriate level of upscaling and then apply it to the whole domain. From the single-phase simulation, the maximum of upscaling is set 8

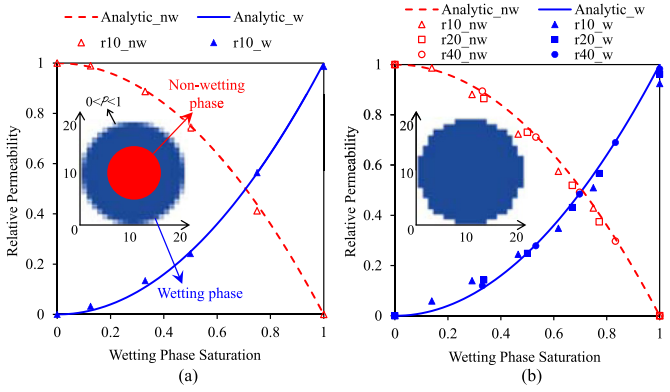

Fig. 5. Relative permeability curve for concurrent annular two-phase flow in a cylindrical tube. (a) Comparison between the VLBM simulation results and analytical solution with the radius of 10 lattice points. (b) Binary-based simulation results with the radii 40, 20, and 10 lattice points.

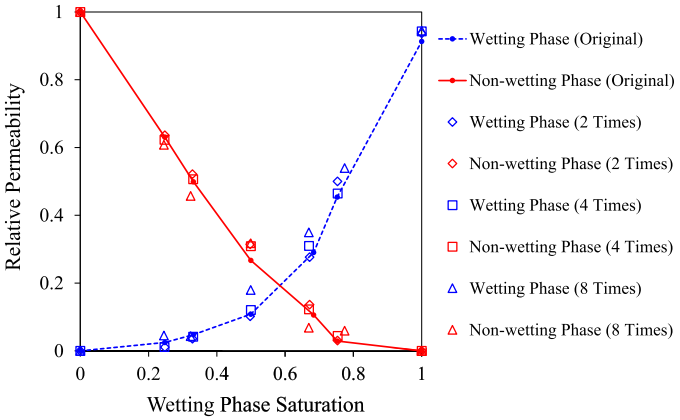

Fig. 6. Relative permeability curve for samples with the sizes of 192 × 192 × 256, 152 × 152 × 203, 120 × 120 × 161 and 96 × 96 × 128. The lines represent the relative curve for the original sample. Different symbols are simulation results of samples with different upscaling levels.

times for the sample used in this paper, with sizes (192 × 192 × 256), (152 × 152 × 203), (120 × 120 × 161) and (96 × 96 × 128), respectively.

In the original and upscaled samples, steady-state two-phase flow is simulated with the following specifications: (a) Two void layers are added in the inlet and outlet boundaries to design periodic boundary. (b) The immiscible two phases are randomly assigned in the pore spaces satisfying specific saturation. (c) The same body force, as a driving force, is applied for both fluids in the flowing direction. (d) Simulation of two-phase flow to reach the steady-state under various saturations. After obtaining the velocity fields, relative permeability curves are analyzed and compared under various saturation.

Fig. 6 illustrates the relative permeability curves for the original sample and the upscaled samples with 2, 4 and 8 times upscaling size. The curves still show a similar tendency even with 8 times coarsened resolutions. At given wetting phase saturation, the relative permeability slightly fluctuates but maintains the main flow characteristics. To guarantee the relative permeability is well retained during pore-scale upscaling, the preferential flow pathways should not change dramatically. Because the preferential flow pathways mainly contribute to the permeability (Thompson et al., 1987). As shown in the bottom row of Fig. 7,

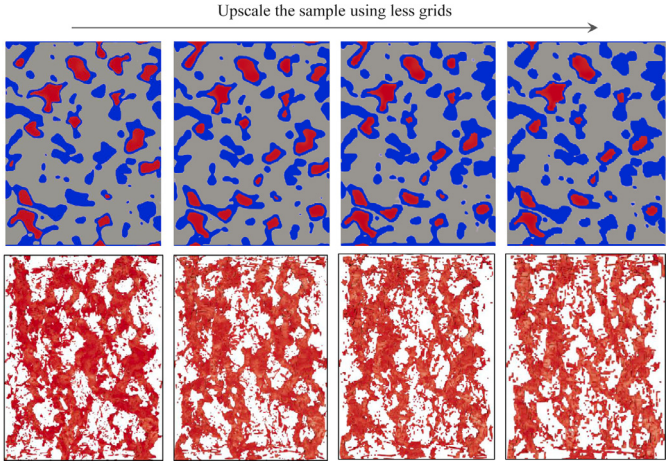

Fig. 7. Comparison between the original and upscaled void space, from left to right, original, 2 × upscaling, 4 × upscaling and 8 × upscaling samples, separately. Top row: distribution of wetting phase (blue) and non-wetting phase (red) in the same slice with about 50% saturation. Bottom row: 2D visualization of the preferential pathways for the non-wetting phase. (For interpretation of the references to colour in this figure legend, the reader is referred to the web version of this article.)

the preferential pathways of the non-wetting phase have almost identical patterns in both upscaled and the original samples.

Porosity, shape of solid boundaries and void space topology control the flow and transport through porous materials. The proposed pore-scale upscaling method ideally preserves the porosity of porous materials by considering the partial occupation of the solid phase in boundary grey cells. The upscaling method maintains smooth solid-interface interface with incidental local porosity, which preserves the original shape of solid-void interfaces. To demonstrate the local effect of upscaling on these properties, 2D slices from different samples are shown in Fig. 7 (top row). After 8-times, the shape of void space is well preserved. We also extract the pore networks for these samples to quantitatively compare the average topology of porous materials. The average coordination number, defined as the number of connected throats for each pore body, is 3.66, 3.65, 3.71 and 3.83 for the original sample and upscaled samples, respectively. As the slight variation in the topology and relative permeability curves in Fig. 6 show, the upscaling does not alter the original results. It should be noted that if the pore size distribution along the preferential pathways is very heterogeneous there are very tight pore spaces as bottle necks, upscaling may need to be taken into account with more cautious.

4. Conclusion

Pore-scale modelling of multi-phase flow and transport in porous materials is one of the main research streamlines in industry and fundamental research. This research presents a fundamental computational study that contributes to this topic with three different aspects:

a. The concept of volumetric lattice Boltzmann method is combined with the Shan-Chen two-phase model. For the streaming part, particle bounce back is considered at the solid boundaries. In addition, the force term is modified by adding the weighting factor of the solid ratio. The volumetric lattice Boltzmann method for two-phase flow inherits the features of LBM that are conducive to parallelism.
b. Level-set method can provide the details of boundaries' location. With local refinement method, the solid ratio is calculated for every cell, which seamlessly fed into the VLBM method.
c. All the computational methods in (a) and (b) have been applied in a GPU-based framework which allows parallelization of the results. This is an important aspect of this study as it allows to simulation much larger physical scales at a shorter computational time.
d. The pore-scale upscaling method is proposed for the image-based simulation. To decrease the computational demand while maintaining accuracy, the continuous solid ratio is used to average the adjacent cells. The upscaled data set can still retain the topology of the pore structure, especially for bigger channels. The numerical method for upscaling was validated against the annular two-phase flow and compared against the analytical solution. Then, it was applied to steady-state relative permeability study and it was shown that for the specific medium up to 8 times coarsening did not change the relative permeability results while saving significant computational cost.

The upscaling scheme is restricted by the smallest pore as well as pores in the main flow pathways. In future studies, we aim to enhance the upscaling method depending on the local pore-size distribution.

Declaration of Competing Interest

The authors declare that they have no known competing financial interests or personal relationships that could have appeared to influence the work reported in this paper.

CRediT authorship contribution statement

Senyou An: Conceptualization, Software, Investigation, Writing - original draft, Writing - review & editing. **Yuting Zhan:** Investigation, Writing - original draft, Writing - review & editing. **Jun Yao:** Conceptualization, Investigation, Writing - original draft, Writing - review & editing. **Huidan Whitney Yu:** Investigation, Writing - original draft, Writing - review & editing. **Vahid Niasar:** Funding acquisition, Supervision, Writing - original draft, Writing - review & editing.

Acknowledgments

This research was supported by President's Doctoral Scholar Award of the University of Manchester awarded to Senyou An, Imperial College London and the China Scholar-ship Council (CSC) financial support to Yuting Zhan. After publication, the readers can find the data that support the figures and conclusions presented in the manuscript in the Mendeley repository with the doi: 10.17632/5rcpb43g4w.2.

References

An, S., Hasan, S., Erfani, H., Babaei, M., Niasar, V., 2020. Unravelling effects of the pore-size correlation length on the two-phase flow and solute transport properties; GPU-based pore-network modelling. Water Resources Res.
An, S., Yao, J., Yang, Y., et al., 2016. Influence of pore structure parameters on flow characteristics based on a digital rock and the pore network model. J. Nat. Gas Sci. Eng. 31, 156–163.
An, S., Yu, H.W., Wang, Z., Kapadia, B., Yao, J., 2017. Unified mesoscopic modeling and GPU-accelerated computational method for image-based pore-scale porous media flows. Int. J. Heat Mass Transf. 115, 1192–1202.
An, S., Yu, H.W., Yao, J., 2017. GPU-accelerated volumetric lattice boltzmann method for porous media flow. J. Pet. Sci. Eng. 156, 546–552.
Aziz, R., Joekar-Niasar, V., Martinez-Ferrer, P., 2018. Pore-scale insights into transport and mixing in steady-state two-phase flow in porous media. Int. J. Multiphase Flow 109, 51–62.
Bakke, S., Øren, P.E., et al., 1997. 3-d pore-scale modelling of sandstones and flow simulations in the pore networks. SPE J. 2, 136–149.
Boek, E.S., Venturoli, M., 2010. Lattice-boltzmann studies of fluid flow in porous media with realistic rock geometries. Comput. Math. Appl. 59, 2305–2314.
Bruant Jr, R. G., Celia, M. A., Guswa, A. J., Peters, C. A., 2002. Peer reviewed: safe storage of CO2 in deep saline aquifiers.
Christie, M., Blunt, M., et al., 2001. Tenth SPE comparative solution project: a comparison of upscaling techniques. SPE Reservoir Simulation Symposium. Society of Petroleum Engineers.
Christie, M.A., et al., 1996. Upscaling for reservoir simulation. J. Pet. Technol. 48, 1–004.
Cornelissen, P., Leijnse, A., Joekar-Niasar, V., van der Zee, S., 2019. Pressure development in charged porous media with heterogeneous pore sizes. Adv. Water Resour. 128, 193–205.
Dunsmuir, J.H., Ferguson, S., D'Amico, K., Stokes, J., et al., 1991. X-ray microtomography: a new tool for the characterization of porous media. In: SPE Annual Technical Conference and Exhibition. Society of Petroleum Engineers.
Fatt, I., et al., 1956. The network model of porous media.
Ferreol, B., Rothman, D.H., 1995. Lattice-boltzmann simulations of flow through fontainebleau sandstone. In: Multiphase Flow in Porous Media. Springer, pp. 3–20.
Gao, Y., Lin, Q., Bijeljic, B., Blunt, M.J., 2017. X-ray microtomography of intermittency in multiphase flow at steady state using a differential imaging method. Water Resour. Res. 53, 10274–10292.
Gelfand, B., Ambati, J., An, S., Chen, R., Whitney, H.Y., Yao, J., 2018. Hemodynamic shear stress in the inner choroid primes endothelium for complement damage. Invest. Ophthalmol. Vis. Sci. 59, 3473.
Genty, A., Pot, V., 2013. Numerical simulation of 3d liquid–gas distribution in porous media by a two-phase TRT lattice boltzmann method. Transp. Porous Media 96, 271–294.
Godine-Brizuela, O.E., Niasar, V.J., 2019. Simultaneous pressure and electro-osmosis driven flow in charged porous media: pore-scale effects on mixing and dispersion. J. Colloid Interface Sci..
Godinez-Brizuela, O.E., Karadimitriou, N.K., Joekar-Niasar, V., Shore, C.A., Oostrom, M., 2017. Role of corner interfacial area in uniqueness of capillary pressure-saturation-interfacial area relation under transient conditions. Adv. Water Resour. 107, 10–21.
Guo, Z., Shi, B., Wang, N., 2000. Lattice BGK model for incompressible Navier–Stokes equation. J. Comput. Phys. 165, 288–306.
Guo, Z., Zheng, C., Shi, B., 2002. An extrapolation method for boundary conditions in lattice boltzmann method. Phys. Fluids 14, 2007–2010.
Hasan, S., Joekar-Niasar, V., Karadimitriou, N.K., Sahimi, M., 2019. Saturation-dependence of non-fickian transport in porous media. Water Resour. Res..
Huang, H., Sukop, M., Lu, X., 2015. Multiphase Lattice Boltzmann Methods: Theory and Application. John Wiley & Sons.
Huang, H., Thorne Jr, D.T., Schaap, M.G., Sukop, M.C., 2007. Proposed approximation for contact angles in Shan-and-Chen-type multicomponent multiphase lattice boltzmann models. Phys. Rev. E 76, 066701.
Joekar-Niasar, V., van Dijke, M.I., Hassanizadeh, S.M., 2012. Pore-scale modeling of multiphase flow and transport: achievements and perspectives. Transp. Porous Media 1–4.

Joekar-Niasar, V., Hassanizadeh, S., 2012. Analysis of fundamentals of two-phase flow in porous media using dynamic pore-network models: a review. Crit. Rev. Environ. Sci. Technol. 42, 1895–1976.
Joekar-Niasar, V., Hassanizadeh, S.M., Dahle, H., 2010. Non-equilibrium effects in capillarity and interfacial area in two-phase flow: dynamic pore-network modelling. J. Fluid Mech. 655, 38–71.
Karadimitriou, N.K., Joekar-Niasar, V., Brizuela, O.G., 2017. Hydro-dynamic solute transport under two-phase flow conditions. Sci. Rep. 7, 6624.
Katz, N.M., 2016. Gauss Sums, Kloosterman Sums, and Monodromy Groups.(AM-116), vol. 116. Princeton university press.
Li, W., Wei, X., Kaufman, A., 2003. Implementing lattice boltzmann computation on graphics hardware. Vis. Comput. 19, 444–456.
Martys, N.S., Chen, H., 1996. Simulation of multicomponent fluids in complex three-dimensional geometries by the lattice boltzmann method. Phys. Rev. E 53, 743.
Masoodi, R., Pillai, K.M., 2012. Wicking in Porous Materials: Traditional and Modern Modeling Approaches. CRC Press.
Mitiche, A., Ayed, I.B., 2010. Variational and Level Set Methods in Image Segmentation. Springer Science & Business Media.
Niblett, D., Joekar-Niasar, V., Holmes, S., 2019. Enhancing the performance of fuel cell gas diffusion layers using ordered microstructural design. J. Electrochem. Soc..
Ollivier-Gooch, C., Altena, M.V., 2002. A high-order-accurate unstructured mesh finite-volume scheme for the advection–diffusion equation. J. Comput. Phys. 181, 729–752.
Pan, C., Hilpert, M., Miller, C., 2004. Lattice-boltzmann simulation of two-phase flow in porous media. Water Resour. Res. 40.
Premnath, K.N., Abraham, J., 2007. Three-dimensional multi-relaxation time (MRT) lattice-boltzmann models for multiphase flow. J. Comput. Phys. 224, 539–559.
Raeini, A.Q., Bijeljic, B., Blunt, M.J., 2015. Modelling capillary trapping using finite-volume simulation of two-phase flow directly on micro-ct images. Adv. Water Resour. 83, 102–110.
Raeini, A.Q., Blunt, M.J., Bijeljic, B., 2012. Modelling two-phase flow in porous media at the pore scale using the volume-of-fluid method. J. Comput. Phys. 231, 5653–5668.
Raeini, A.Q., Blunt, M.J., Bijeljic, B., 2014. Direct simulations of two-phase flow on micro-ct images of porous media and upscaling of pore-scale forces. Adv. Water Resour. 74, 116–126.
Ramstad, T., Idowu, N., Nardi, C., Øren, P.E., 2012. Relative permeability calculations from two-phase flow simulations directly on digital images of porous rocks. Transp. Porous Media 94, 487–504.
Ramstad, T., Øren, P.-E., Bakke, S., et al., 2010. Simulation of two-phase flow in reservoir rocks using a lattice boltzmann method. SPE J. 15, 917–927.
Salehi, A., Voskov, D.V., Tchelepi, H.A., et al., 2019. K-values-based upscaling of compositional simulation. SPE J. 24, 579–595.
Sethian, J.A., 1999. Level Set Methods and Fast Marching Methods: Evolving Interfaces in Computational Geometry, Fluid Mechanics, Computer Vision, and Materials Science, vol. 3. Cambridge university press.
Shan, X., Doolen, G., 1995. Multicomponent lattice-boltzmann model with interparticle interaction. J. Stat. Phys. 81, 379–393.
Taylor, C., Hood, P., 1973. A numerical solution of the Navier-Stokes equations using the finite element technique. Comput. Fluids 1, 73–100.
Thompson, A., Katz, A., Krohn, C., 1987. The microgeometry and transport properties of sedimentary rock. Adv. Phys. 36, 625–694.
Tracy, S.R., Daly, K.R., Sturrock, C.J., Crout, N.M., Mooney, S.J., Roose, T., 2015. Three--dimensional quantification of soil hydraulic properties using x-ray computed tomography and image-based modeling. Water Resour. Res. 51, 1006–1022.
Wang, Y., Chung, T., Armstrong, R., McClure, J., Ramstad, T., Mostaghimi, P., 2020. Accelerated computation of relative permeability by coupled morphological and direct multiphase flow simulation. J. Comput. Phys. 401, 108966.
Wang, Z., Yan, Z., Chen, G., 2011. Lattice boltzmann method of active contour for image segmentation. In: 2011 Sixth International Conference on Image and Graphics. IEEE, pp. 338–343.
Wang, Z., Zhao, Y., Sawchuck, A.P., Dalsing, M.C., Yu, H.W., 2015. GPU acceleration of volumetric lattice boltzmann method for patient-specific computational hemodynamics. Comput. Fluids 115, 192–200.
Xiong, Q., Baychev, T.G., Jivkov, A.P., 2016. Review of pore network modelling of porous media: experimental characterisations, network constructions and applications to reactive transport. J. Contam. Hydrol. 192, 101–117.
Yang, Y., Tao, L., Yang, H., Iglauer, S., Wang, X., Askari, R., Yao, J., Zhang, K., Zhang, L., Sun, H., 2020. Stress sensitivity of fractured and vuggy carbonate: an x-ray computed tomography analysis. J. Geophys. Res. Solid Earth.
Yin, X., Zhang, J., 2012. An improved bounce-back scheme for complex boundary conditions in lattice boltzmann method. J. Comput. Phys. 231, 4295–4303.
Yu, H., Chen, X., Wang, Z., Deep, D., Lima, E., Zhao, Y., Teague, S.D., 2014. Mass-conserved volumetric lattice boltzmann method for complex flows with willfully moving boundaries. Phys. Rev. E 89, 063304.
Zhao, J., Yao, J., Zhang, M., et al., 2016. Study of gas flow characteristics in tight porous media with a microscale lattice boltzmann model. Sci. Rep. 6, 32393.